Available online at www.sciencedirect.com
ScienceDirect
International Journal of Heat and Mass Transfer 51 (2008) 3486–3503
International Journal of HEAT and MASS TRANSFER
www.elsevier.com/locate/ijhmt

Role of 'Bejan's heatlines' in heat flow visualization and optimal thermal mixing for differentially heated square enclosures

Tanmay Basak [a], S. Roy [b,*]

[a] Department of Chemical Engineering, Indian Institute of Technology Madras, Chennai 600036, India
[b] Department of Mathematics, Indian Institute of Technology Madras, Chennai 600036, India

Received 7 May 2007; received in revised form 10 October 2007
Available online 22 January 2008

Abstract

Heat flow patterns in the presence of natural convection have been analyzed with Bejan's heatlines concept. Momentum and energy transfer are characterized by streamfunctions and heatfunctions, respectively such that streamfunctions and heatfunctions satisfy the dimensionless forms of momentum and energy balance equations, respectively. Finite element method has been used to solve the velocity and thermal fields and the method has also been found robust to obtain the streamfunction and heatfunction accurately. The unique solution of heatfunctions for situations in differential heating is a strong function of Dirichlet boundary condition which has been obtained from average Nusselt numbers for hot or cold regimes. The physical significance of heatlines have been demonstrated for a comprehensive understanding of energy distribution and optimal thermal management via analyzing three cases. Case 1 involves the uniform and non-uniform heating of bottom wall with cooled side walls. The studies illustrate that the heat flow primarily occurs from the central regime of the bottom wall to a very small regime of the top portion of side walls. A large portion of central regime of cold side walls do not receive significant amount of heat. In order to maximize the thermal energy distribution, the distributed heating at the middle portions of the bottom and side walls have been considered in case 2 and heatlines clearly depict the distributions of heat from the hot walls to the large regimes of the cold wall. Further case 3 illustrates the enhanced heat flows in presence of heated bottom and left side walls. Heatline is found as an effective numerical tool to visualize energy distribution in order to establish a suitable heating strategy.

Keywords: Heatlines; Heatfunctions; Streamlines; Streamfunctions; Natural convection; Square cavity; Uniform and non-uniform heating

1. Introduction

Natural convection in enclosed cavities has received significant attention due to many engineering applications [1–3]. Steady natural convection within a differentially heated square enclosure has a major role in food preservation at an optimal temperature. Analysis of food sterilization in various cavities has also been studied by earlier investigators [4,5].

Investigations of natural convection in a square enclosure has been carried out for past two decades by several investigators (Patterson and Imberger [6], Nicolette et al. [7], Hall et al. [8], Hyun and Lee [9], Fusegi et al. [10], Lage and Bejan [11,12], and Xia and Murthy [13]). November and Nansteel [14] and Valencia and Frederick [15] have shown a specific interest to focus on a natural convection within a rectangular enclosure wherein a bottom heating and/or a top cooling are involved. Studies on natural convection in rectangular enclosures heated from below and cooled along a single side or both sides have been carried out by Ganzarolli and Milanez [16]. Kimura and Bejan [17] also studied natural convection in differentially heated corner region. They established that the flow field is relatively insensitive to whether the wall temperature varies continuously or discontinuously through the corner point. Later, the case of heating from one side and cooling from

* Corresponding author.
E-mail addresses: tanmay@iitm.ac.in (T. Basak), sjroy@iitm.ac.in (S. Roy).

0017-9310/$ - see front matter © 2007 Elsevier Ltd. All rights reserved.
doi:10.1016/j.ijheatmasstransfer.2007.10.033

Nomenclature

g	acceleration due to gravity, m s^{-2}
k	thermal conductivity, W m^{-1} K^{-1}
L	side of the square cavity, m
N	total number of nodes
p	pressure, Pa
P	dimensionless pressure
Pr	Prandtl number
R	residual of weak form
Ra	Rayleigh number
T	temperature, K
T_h	temperature of hot bottom wall, K
T_c	temperature of cold vertical wall, K
u	x component of velocity
U	x component of dimensionless velocity
v	y component of velocity
V	y component of dimensionless velocity
X	dimensionless distance along x coordinate
x	distance along x coordinate
Y	dimensionless distance along y coordinate
y	distance along y coordinate

Greek symbols

α	thermal diffusivity, m^2 s^{-1}
β	volume expansion coefficient, K^{-1}
γ	penalty parameter
Γ	boundary
θ	dimensionless temperature
ν	kinematic viscosity, m^2 s^{-1}
ρ	density, kg m^{-3}
Φ	basis functions
ψ	streamfunction
Π	heatfunction

Subscripts

i	residual number
k	node number

the top has been analyzed by Aydin et al. [18] who investigated the influence of aspect ratio for air-filled rectangular enclosures. Also, Kirkpatrick and Bohn [19] examined experimentally the case of high Rayleigh number natural convection in a water-filled cubical enclosure heated simultaneously from below and from the side. Corcione [20] studied natural convection in a air-filled rectangular enclosure heated from below and cooled from above for a variety of thermal boundary conditions at the side walls. Numerical results were reported for several values of both width-to-height aspect ratio of the enclosure and Rayleigh number. Recently, Basak et al. [21] and Roy and Basak [22] investigated natural convection within a square enclosure for hot bottom wall and various hot/cold side walls with insulated top wall. However, optimal heating policies for all these situations have not been reported. Current work fills the gap by analyzing the 'Bejan's heatlines' for visualizing energy flow due to natural convection in a square enclosure.

The heatline is the best way to visualize the heat transfer in two dimensional convective transport processes. The streamlines are the best tools to visualize the fluid motions in two dimensional incompressible flow. Similarly, the heatlines, which are also heat flux lines, represent the trajectory of heat energy. In general, the heat flux lines are normal to the isotherms for heat transfer due to pure conduction through isotropic media. Energy flow within various regimes especially for convective heat transport processes can be best visualized by heatlines whereas isotherms are unable to give guideline for energy flows. The heatlines are mathematically represented by heatfunctions and the proper dimensionless forms of heatfunctions are closely related to overall Nusselt numbers.

The heatline concept was first introduced by Kimura and Bejan [23] and Bejan [24]. Various applications were further studied by Bello-Ochende [25], Costa [26–29] and Deng and Tang [30]. Bejan [31] also reviewed some earlier works on heatlines and illustrated the use of heatline concept to visualize various physical situations. Till date, the heatline concept has not been used extensively for analyzing convective heat transport processes except for very few applications. Application of heatlines was shown for thermomagnetic convection in electroconductive melts [32,33]. The heatline concept was further used for unsteady heat transfer assuming that steady state version of energy balance equation is satisfied at a given instant [34]. Application of heatlines have also been carried out for investigations in polar coordinates [35–39]. The heatline concept has also been applied for analyzing heat transfer involving forced convection [40,41] and turbulent flows [42].

The aim of this article is to analyze energy flows due to natural convection in a square enclosure with hot bottom wall and cold side walls in presence of insulated top walls. The main objective of this fundamental study is to examine thermal mixing near the central core of the cavity especially for food processing applications. Further, the influence of distributed heat source will be investigated to enhance thermal mixing via the trajectory of heat flow using 'Bejan's heatlines' concept. The thermal mixing and heat flow will also be investigated for two adjacent hot walls with a cold side wall in presence of insulated top wall. In the current study, we have used Galerkin finite element method with penalty parameter to solve the non-linear coupled partial differential equations of flow and temperature fields. The Galerkin method is further employed to solve the Poisson equation for streamfunctions and heatfunctions. It may

be noted that Galerkin finite element method has been used here for the first time to evaluate the heatfunction. The junction of hot and cold walls correspond to mathematical singularity which is quite common for many practical situations. The heatfunctions for such type of situations involve implementation of exact boundary conditions at those singular points. Current work analyzes series of such practical problems as a first attempt and generic boundary conditions on heatfunctions have been derived based on overall heat balance and average Nusselt numbers on hot and cold walls. The heatlines and thermal mixing will be illustrated for commonly used fluid with $Pr = 0.7$–1000 in various industrial applications.

2. Mathematical formulation and simulation

2.1. Velocity and temperature distributions

The physical domain is shown in Fig. 1. Thermophysical properties of the fluid in the flow field are assumed to be constant except the density variations causing a body force term in the vertical component of momentum equation. The Boussinesq approximation is invoked for the fluid properties due to the variation of density with temperature and the density variation cause a body force in the vertical momentum equation as given below. Therefore, the temperature field is coupled to the flow field via the body force term. Under these assumptions governing equations for steady two-dimensional natural convection flow in the square cavity using conservation of mass, momentum and energy can be written with following dimensionless variables or numbers

$$X = \frac{x}{L}, \quad Y = \frac{y}{L}, \quad U = \frac{uL}{\alpha}, \quad V = \frac{vL}{\alpha}, \quad \theta = \frac{T - T_c}{T_h - T_c},$$
$$P = \frac{pL^2}{\rho\alpha^2}, \quad Pr = \frac{v}{\alpha}, \quad Ra = \frac{g\beta(T_h - T_c)L^3 Pr}{v^2} \tag{1}$$

as:

$$\frac{\partial U}{\partial X} + \frac{\partial V}{\partial Y} = 0, \tag{2}$$

$$U\frac{\partial U}{\partial X} + V\frac{\partial U}{\partial Y} = -\frac{\partial P}{\partial X} + Pr\left(\frac{\partial^2 U}{\partial X^2} + \frac{\partial^2 U}{\partial Y^2}\right), \tag{3}$$

$$U\frac{\partial V}{\partial X} + V\frac{\partial V}{\partial Y} = -\frac{\partial P}{\partial Y} + Pr\left(\frac{\partial^2 V}{\partial X^2} + \frac{\partial^2 V}{\partial Y^2}\right) + RaPr\theta, \tag{4}$$

$$U\frac{\partial \theta}{\partial X} + V\frac{\partial \theta}{\partial Y} = \frac{\partial^2 \theta}{\partial X^2} + \frac{\partial^2 \theta}{\partial Y^2} \tag{5}$$

with the boundary conditions for velocities

$$U(X,0) = U(X,1) = U(0,Y) = U(1,Y) = 0,$$
$$V(X,0) = V(X,1) = V(0,Y) = V(1,Y) = 0. \tag{6}$$

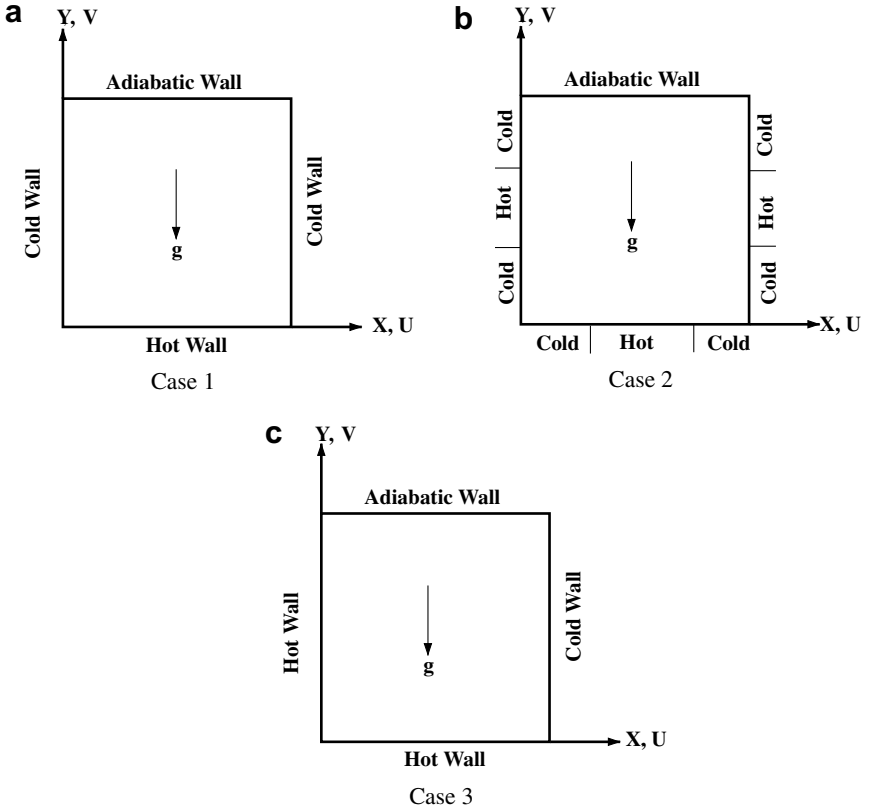

Fig. 1. Schematic diagram of the physical system: (a) case 1: heated bottom wall; (b) case 2: distributed heating at the central regimes of bottom ($0.25 \leqslant X \leqslant 0.75$) and vertical walls ($0.375 \leqslant Y \leqslant 0.625$); (c) case 3: heated bottom and left walls.

The boundary conditions for temperature with cases 1–3 (see Figs. 1a–c) are

$$\begin{aligned}&\theta = 1 \quad \text{(uniform heating) or}\\ &\sin \pi X \text{(non-uniform heating, bottom wall)}\\ &\theta = 0 \quad \text{(for cold wall)}\\ &\frac{\partial \theta}{\partial Y} = 0 \quad \text{(for adiabatic wall)}\end{aligned} \tag{7}$$

Note that, in Eqs. (2)–(7), X and Y are dimensionless coordinates varying along horizontal and vertical directions, respectively; U and V are dimensionless velocity components in the X and Y directions, respectively; θ is the dimensionless temperature; P is the dimensionless pressure; Ra and Pr are Rayleigh and Prandtl numbers, respectively.

The momentum and energy balance equations (Eqs. (3)–(5)) are solved using the Galerkin finite element method. The continuity equation (Eq. (2)) will be used as a constraint due to mass conservation and this constraint may be used to obtain the pressure distribution. In order to solve Eqs. (3) and (4), we use the penalty finite element method where the pressure P is eliminated by a penalty parameter γ and the incompressibility criteria given by Eq. (2) which results in

$$P = -\gamma\left(\frac{\partial U}{\partial X} + \frac{\partial V}{\partial Y}\right). \tag{8}$$

The continuity equation (Eq. (2)) is automatically satisfied for large values of γ. Typical values of γ that yield consistent solutions are 10^7. Using Eq. (8), the momentum balance equations (Eqs. (3) and (4)) reduce to

$$U\frac{\partial U}{\partial X} + V\frac{\partial U}{\partial Y} = \gamma\frac{\partial}{\partial X}\left(\frac{\partial U}{\partial X} + \frac{\partial V}{\partial Y}\right) + Pr\left(\frac{\partial^2 U}{\partial X^2} + \frac{\partial^2 U}{\partial Y^2}\right), \tag{9}$$

and

$$U\frac{\partial V}{\partial X} + V\frac{\partial V}{\partial Y} = \gamma\frac{\partial}{\partial Y}\left(\frac{\partial U}{\partial X} + \frac{\partial V}{\partial Y}\right) + Pr\left(\frac{\partial^2 V}{\partial X^2} + \frac{\partial^2 V}{\partial Y^2}\right) + RaPr\theta. \tag{10}$$

The system of Eqs. (5), (9) and (10) with boundary conditions is solved by using Galerkin finite element method [43]. Expanding the velocity components (U, V) and temperature (θ) using basis set $\{\Phi_k\}_{k=1}^{N}$ as,

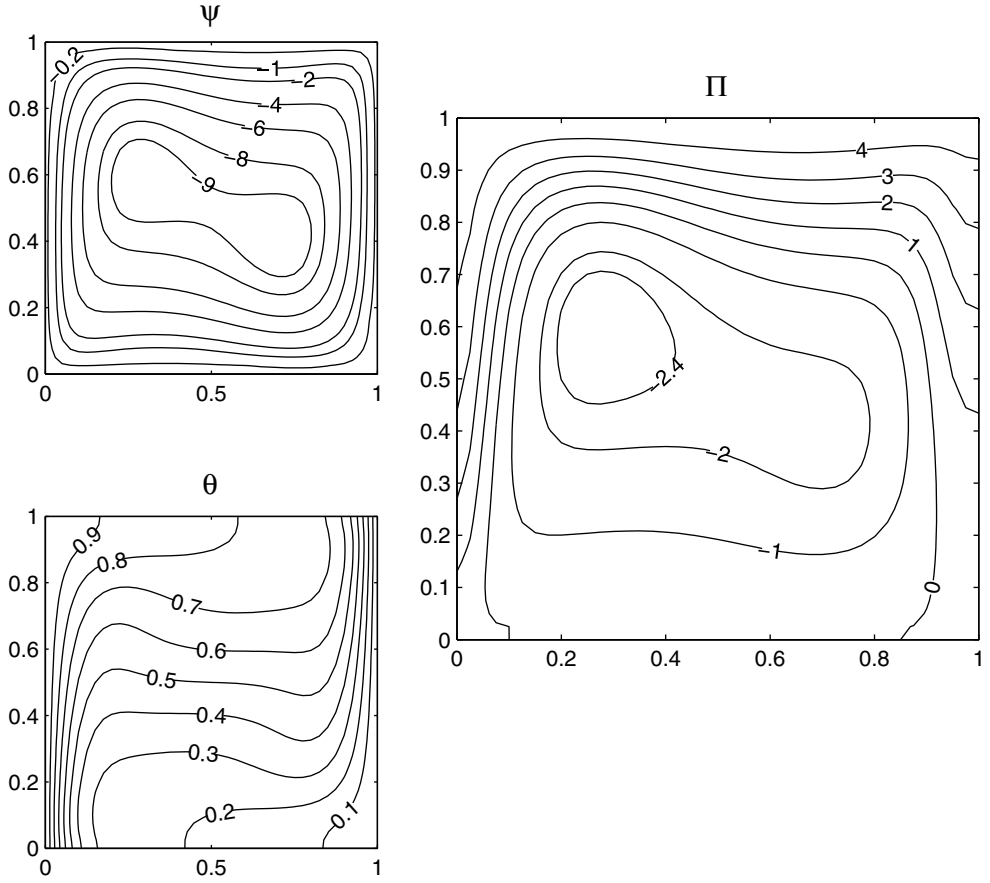

Fig. 2. Streamfunction (ψ), heatfunction (Π) and temperature (θ) contours for heated left wall and cooled right wall with horizontal adiabatic walls with $Pr = 0.71$ and $Ra = 10^5$ (benchmark problem). Clockwise and anti-clockwise flows are shown via negative and positive signs of streamfunctions and heatfunctions, respectively.

$$U \approx \sum_{k=1}^{N} U_k \Phi_k(X,Y),$$

$$V \approx \sum_{k=1}^{N} V_k \Phi_k(X,Y), \quad \text{and} \quad \theta \approx \sum_{k=1}^{N} \theta_k \Phi_k(X,Y), \tag{11}$$

for

$$0 \leqslant X, Y \leqslant 1,$$

the Galerkin finite element method yields the following non-linear residual equations for Eqs. (9), (10) and (5), respectively, at nodes of internal domain Ω:

$$\begin{aligned} R_i^{(1)} = {} & \sum_{k=1}^{N} U_k \int_\Omega \left[\left(\sum_{k=1}^{N} U_k \Phi_k \right) \frac{\partial \Phi_k}{\partial X} \right. \\ & \left. + \left(\sum_{k=1}^{N} V_k \Phi_k \right) \frac{\partial \Phi_k}{\partial Y} \right] \Phi_i \, \mathrm{d}X \, \mathrm{d}Y \\ & + \gamma \left[\sum_{k=1}^{N} U_k \int_\Omega \frac{\partial \Phi_i}{\partial X} \frac{\partial \Phi_k}{\partial X} \, \mathrm{d}X \, \mathrm{d}Y \right. \\ & \left. + \sum_{k=1}^{N} V_k \int_\Omega \frac{\partial \Phi_i}{\partial X} \frac{\partial \Phi_k}{\partial Y} \, \mathrm{d}X \, \mathrm{d}Y \right] \\ & + Pr \sum_{k=1}^{N} U_k \int_\Omega \left[\frac{\partial \Phi_i}{\partial X} \frac{\partial \Phi_k}{\partial X} + \frac{\partial \Phi_i}{\partial Y} \frac{\partial \Phi_k}{\partial Y} \right] \mathrm{d}X \, \mathrm{d}Y \end{aligned} \tag{12}$$

$$\begin{aligned} R_i^{(2)} = {} & \sum_{k=1}^{N} V_k \int_\Omega \left[\left(\sum_{k=1}^{N} U_k \Phi_k \right) \frac{\partial \Phi_k}{\partial X} \right. \\ & \left. + \left(\sum_{k=1}^{N} V_k \Phi_k \right) \frac{\partial \Phi_k}{\partial Y} \right] \Phi_i \, \mathrm{d}X \, \mathrm{d}Y \\ & + \gamma \left[\sum_{k=1}^{N} U_k \int_\Omega \frac{\partial \Phi_i}{\partial Y} \frac{\partial \Phi_k}{\partial X} \, \mathrm{d}X \, \mathrm{d}Y \right. \\ & \left. + \sum_{k=1}^{N} V_k \int_\Omega \frac{\partial \Phi_i}{\partial Y} \frac{\partial \Phi_k}{\partial Y} \, \mathrm{d}X \, \mathrm{d}Y \right] \\ & + Pr \sum_{k=1}^{N} V_k \int_\Omega \left[\frac{\partial \Phi_i}{\partial X} \frac{\partial \Phi_k}{\partial X} + \frac{\partial \Phi_i}{\partial Y} \frac{\partial \Phi_k}{\partial Y} \right] \mathrm{d}X \, \mathrm{d}Y \\ & - RaPr \int_\Omega \left(\sum_{k=1}^{N} \theta_k \Phi_k \right) \Phi_i \, \mathrm{d}X \, \mathrm{d}Y \end{aligned} \tag{13}$$

and

$$\begin{aligned} R_i^{(3)} = {} & \sum_{k=1}^{N} \theta_k \int_\Omega \left[\left(\sum_{k=1}^{N} U_k \Phi_k \right) \frac{\partial \Phi_k}{\partial X} + \left(\sum_{k=1}^{N} V_k \Phi_k \right) \frac{\partial \Phi_k}{\partial Y} \right] \Phi_i \, \mathrm{d}X \, \mathrm{d}Y \\ & + \sum_{k=1}^{N} \theta_k \int_\Omega \left[\frac{\partial \Phi_i}{\partial X} \frac{\partial \Phi_k}{\partial X} + \frac{\partial \Phi_i}{\partial Y} \frac{\partial \Phi_k}{\partial Y} \right] \mathrm{d}X \, \mathrm{d}Y. \end{aligned} \tag{14}$$

Bi-quadratic basis functions with three point Gaussian quadrature is used to evaluate the integrals in the residual

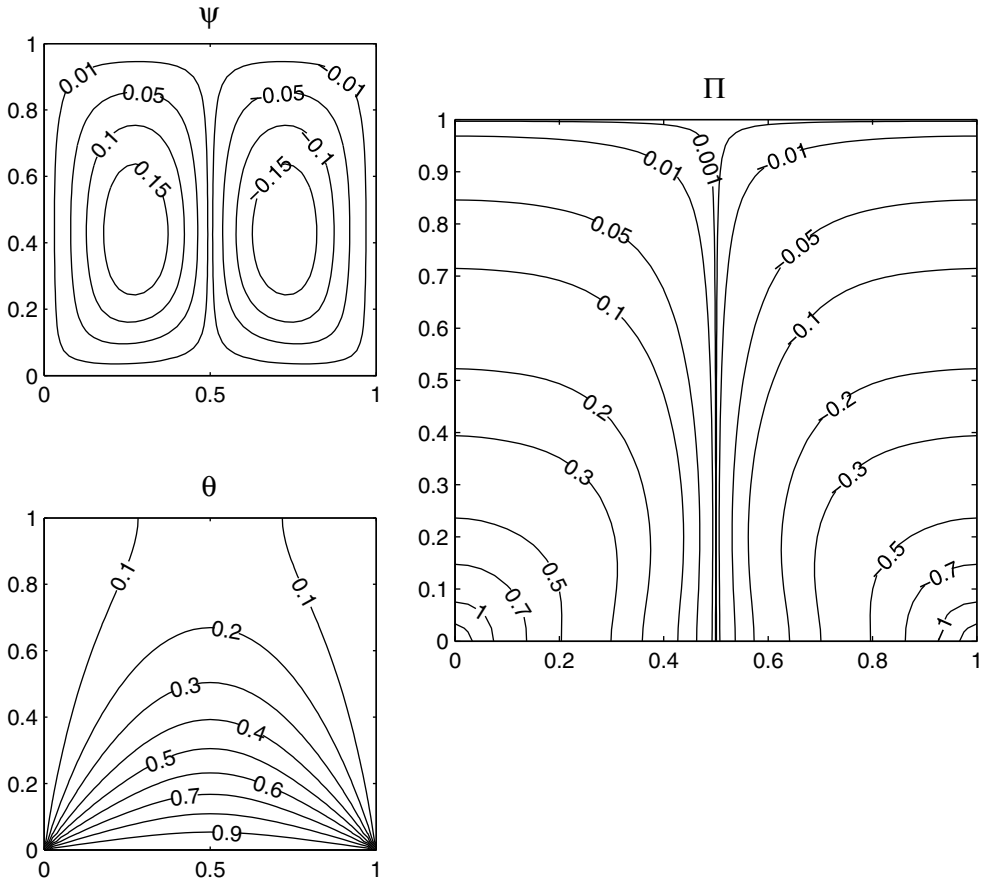

Fig. 3. Streamfunction (ψ), heatfunction (Π) and temperature (θ) contours for uniform heating corresponding to case 1 with $Pr = 0.026$ and $Ra = 10^3$. Clockwise and anti-clockwise flows are shown via negative and positive signs of streamfunctions and heatfunctions, respectively.

equations. In Eqs. (12) and (13), the terms containing the penalty parameter (γ) are evaluated with two point Gaussian quadrature (reduced integration penalty formulation, Reddy [43]). The non-linear residual Eqs. (12)–(14) are solved using Newton–Raphson procedure to determine the coefficients of the expansions in Eq. (11). The detailed solution procedure may be found in earlier works [21,22].

2.2. Streamfunction and heatfunction

The fluid motion is displayed using the streamfunction ψ obtained from velocity components U and V. The relationships between streamfunction, ψ [44] and velocity components for two dimensional flows are

$$U = \frac{\partial \psi}{\partial Y} \quad \text{and} \quad V = -\frac{\partial \psi}{\partial X}, \tag{15}$$

which yield a single equation

$$\frac{\partial^2 \psi}{\partial X^2} + \frac{\partial^2 \psi}{\partial Y^2} = \frac{\partial U}{\partial Y} - \frac{\partial V}{\partial X}. \tag{16}$$

Using the above definition of the streamfunction, the positive sign of ψ denotes anti-clockwise circulation and the clockwise circulation is represented by the negative sign of ψ. Expanding the streamfunction (ψ) using the basis set $\{\Phi\}$ as $\psi = \sum_{k=1}^{N} \psi_k \Phi_k(X, Y)$ and the relation for U and V from Eq. (11), the Galerkin finite element method yields the following linear residual equations for Eq. (16).

$$\begin{aligned} R_i^s = & \sum_{k=1}^{N} \psi_k \int_\Omega \left[\frac{\partial \Phi_i}{\partial X} \frac{\partial \Phi_k}{\partial X} + \frac{\partial \Phi_i}{\partial Y} \frac{\partial \Phi_k}{\partial Y} \right] \mathrm{d}X\,\mathrm{d}Y \\ & - \int_\Gamma \Phi_i \mathbf{n} \cdot \nabla \psi \,\mathrm{d}\Gamma + \sum_{k=1}^{N} U_k \int_\Omega \Phi_i \frac{\partial \Phi_k}{\partial Y} \,\mathrm{d}X\,\mathrm{d}Y \\ & - \sum_{k=1}^{N} V_k \int_\Omega \Phi_i \frac{\partial \Phi_k}{\partial X} \,\mathrm{d}X\,\mathrm{d}Y. \end{aligned} \tag{17}$$

The no-slip condition is valid at all boundaries as there is no cross flow, hence $\psi = 0$ is used as residual equations at the nodes for the boundaries. The bi-quadratic basis function is used to evaluate the integrals in Eq. (17) and ψ's are obtained by solving the N linear residual Eq. (17).

The heat flow within the enclosure is displayed using the heatfunction Π obtained from conductive heat fluxes $\left(-\frac{\partial \theta}{\partial X}, -\frac{\partial \theta}{\partial Y}\right)$ as well as convective heat fluxes ($U\theta$, $V\theta$). The heatfunction satisfies the steady energy balance equation (Eq. (5)) [23] such that

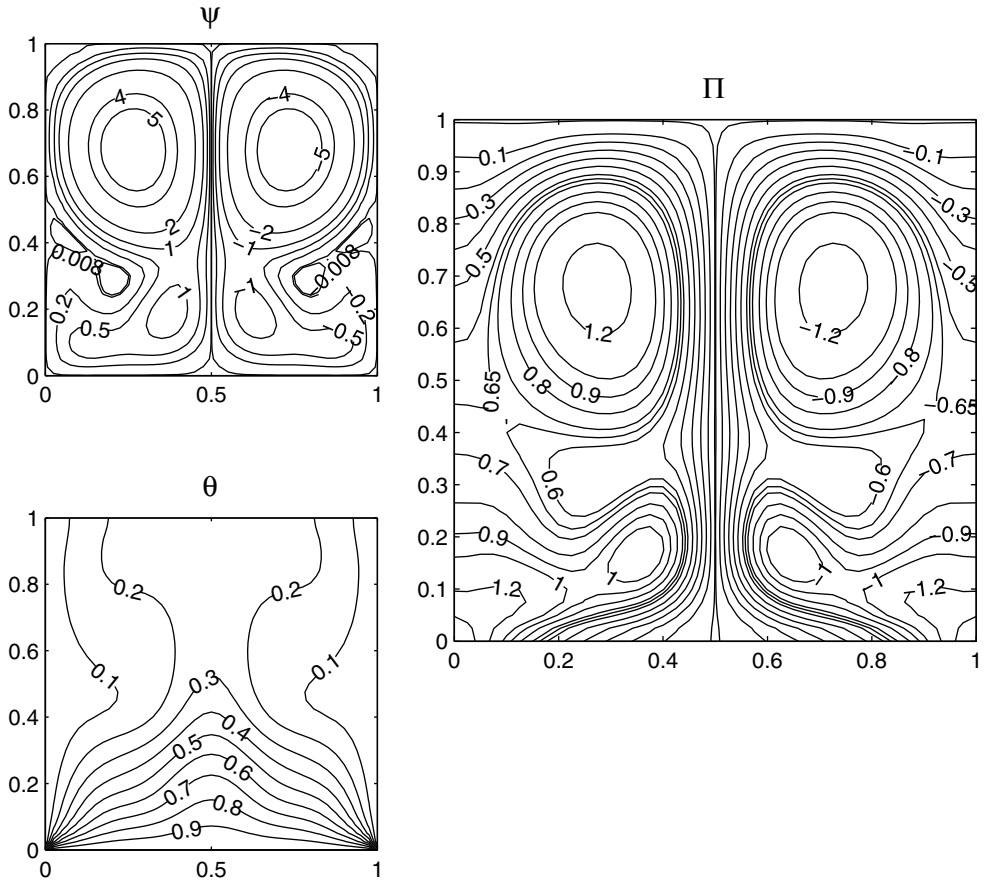

Fig. 4. Streamfunction (ψ), heatfunction (Π) and temperature (θ) contours for uniform heating corresponding to case 1 with $Pr = 0.026$ and $Ra = 10^5$. Clockwise and anti-clockwise flows are shown via negative and positive signs of streamfunctions and heatfunctions, respectively.

$$\frac{\partial \Pi}{\partial Y} = U\theta - \frac{\partial \theta}{\partial X}, \qquad -\frac{\partial \Pi}{\partial X} = V\theta - \frac{\partial \theta}{\partial Y} \tag{18}$$

which yield a single equation

$$\frac{\partial^2 \Pi}{\partial X^2} + \frac{\partial^2 \Pi}{\partial Y^2} = \frac{\partial}{\partial Y}(U\theta) - \frac{\partial}{\partial X}(V\theta). \tag{19}$$

Using the above definition of the heatfunction, the positive sign of Π denotes anti-clockwise heat flow and the clockwise heat flow is represented by the negative sign of Π. Expanding the heatfunction (Π) using the basis set $\{\Phi\}$ as $\Pi = \sum_{k=1}^{N} \Pi_k \Phi_k(X, Y)$ and the relation for U, V and θ from Eq. (11), the Galerkin finite element method yields the following linear residual equations for Eq. (19).

$$\begin{aligned} R_i^h = {} & \sum_{k=1}^{N} \Pi_k \int_\Omega \left[\frac{\partial \Phi_i}{\partial X}\frac{\partial \Phi_k}{\partial X} + \frac{\partial \Phi_i}{\partial Y}\frac{\partial \Phi_k}{\partial Y} \right] \mathrm{d}X\,\mathrm{d}Y \\ & - \int_\Gamma \Phi_i \mathbf{n}\cdot\nabla \Pi \,\mathrm{d}\Gamma + \sum_{k=1}^{N} U_k \int_\Omega \left(\sum_{k=1}^{N} \theta_k \Phi_k \right) \Phi_i \frac{\partial \Phi_k}{\partial Y} \mathrm{d}X\,\mathrm{d}Y \\ & + \sum_{k=1}^{N} \theta_k \int_\Omega \left(\sum_{k=1}^{N} U_k \Phi_k \right) \Phi_i \frac{\partial \Phi_k}{\partial Y} \mathrm{d}X\,\mathrm{d}Y \\ & - \sum_{k=1}^{N} V_k \int_\Omega \left(\sum_{k=1}^{N} \theta_k \Phi_k \right) \Phi_i \frac{\partial \Phi_k}{\partial X} \mathrm{d}X\,\mathrm{d}Y \\ & - \sum_{k=1}^{N} \theta_k \int_\Omega \left(\sum_{k=1}^{N} V_k \Phi_k \right) \Phi_i \frac{\partial \Phi_k}{\partial X} \mathrm{d}X\,\mathrm{d}Y \end{aligned} \tag{20}$$

The residual equation (Eq. (20)) is further supplemented with various Dirichlet and Neumann boundary conditions in order to obtain an unique solution of Eq. (19). Neumann boundary conditions for Π are obtained for isothermal (hot or cold) or sinusoidally heated wall as derived from Eq. (18) and the normal derivatives ($\mathbf{n}\cdot\nabla\Pi$) are specified as follows:

(a) for bottom wall

$$\mathbf{n}\cdot\nabla\Pi = 0 \quad \text{(uniform heating)} \qquad = \pi\cos\pi X \quad \text{(sinusoidal heating)} \tag{21}$$

and

(b) for vertical wall

$$\mathbf{n}\cdot\nabla\Pi = 0 \quad \text{(uniform heating or cooling)} \tag{22}$$

The top insulated wall may be represented by Dirichlet boundary condition as obtained from Eq. (18) which is

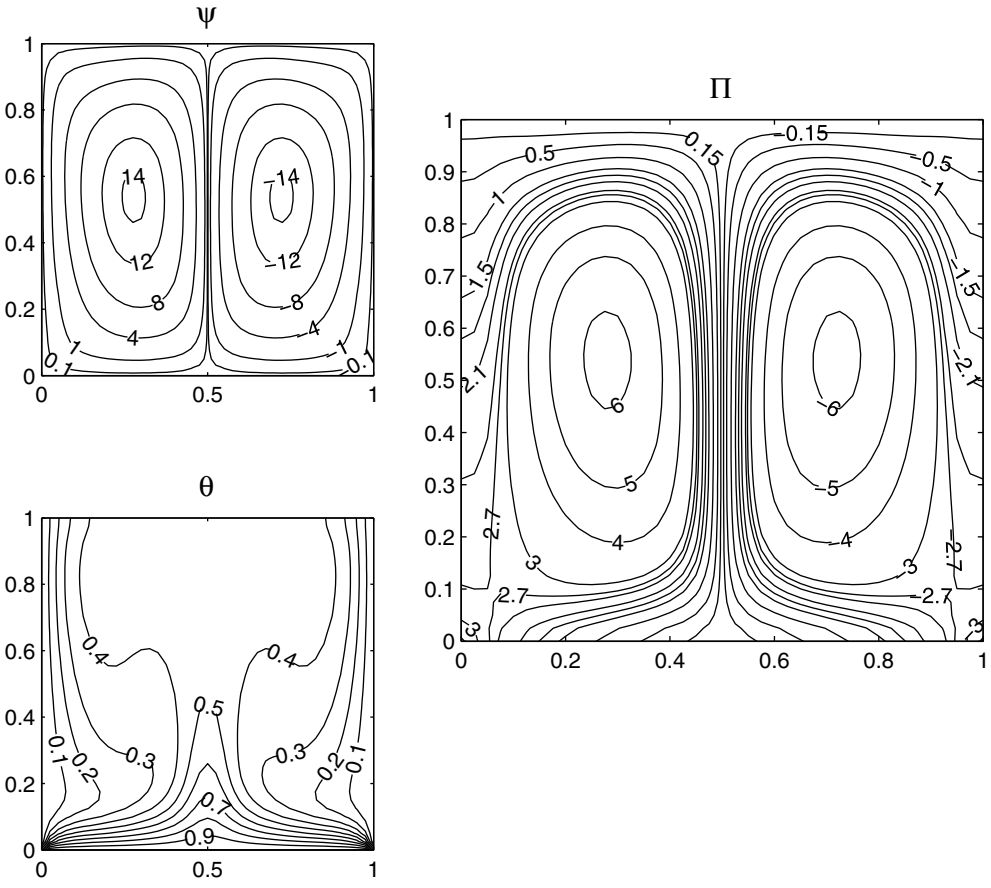

Fig. 5. Streamfunction (ψ), heatfunction (Π) and temperature (θ) contours for uniform heating corresponding to case 1 with $Pr = 0.7$ and $Ra = 10^5$. Clockwise and anti-clockwise flows are shown via negative and positive signs of streamfunctions and heatfunctions, respectively.

simplified into $\frac{\partial \Pi}{\partial X} = 0$ for an adiabatic wall. A reference value of Π is assumed as 0 at $X = 0, Y = 1$ and hence $\Pi = 0$ is valid for $Y = 1, \forall X$. It may be noted that, the unique solution of Eq. (19) is strongly dependent on the non-homogeneous Dirichlet conditions. Most of earlier works [26,30] are limited within two adiabatic walls where Dirichlet boundary condition is either 0 or Nu at the adiabatic walls. Current work is based on the situations of differential heating of walls and Dirichlet conditions for Π have been obtained based on heat flux balance i.e., the total heat gained by the cold wall should be equal to the total heat loss from the hot wall. Therefore, following Dirichlet boundary conditions have been derived for cases 1–3.

(i) case 1:

$$\begin{aligned} \Pi &= \overline{Nu_l}, \quad X = 0, \ Y = 0 \\ &= \overline{Nu_r}, \quad X = 1, \ Y = 0 \end{aligned} \tag{23}$$

(ii) case 2:

$$\begin{aligned} \Pi &= 0.25\overline{Nu_{b,1}}, \ X = 0.25, \ Y = 0 \\ &= 0.25\overline{Nu_{b,3}}, \ X = 0.75, \ Y = 0 \\ &= 0.375\overline{Nu_{l,1}}, \ X = 0, \ Y = 0.375 \\ &= 0.375\overline{Nu_{l,3}}, \ X = 0, \ Y = 0.625 \\ &= 0.375\overline{Nu_{r,1}}, \ X = 1, \ Y = 0.375 \\ &= 0.375\overline{Nu_{r,3}}, \ X = 1, \ Y = 0.625 \end{aligned} \tag{24}$$

(iii) case 3:

$$\Pi = \overline{Nu_r}, \quad X = 1, \ Y = 0 \tag{25}$$

It may be noted that $\overline{Nu_l}$ and $\overline{Nu_r}$ are average Nusselt numbers for left and right walls, respectively for cases 1 and 3. For case 2, $\overline{Nu_{b,1}}, \overline{Nu_{b,3}}$ are average Nusselt numbers for the left and right portions of cold bottom wall, respectively; $\overline{Nu_{l,1}}, \overline{Nu_{l,3}}$ are average Nusselt numbers for the bottom and top portions of cold left wall, respectively and $\overline{Nu_{r,1}}, \overline{Nu_{r,3}}$ are average Nusselt numbers for the bottom and top portions of cold right wall, respectively.

3. Results and discussion

3.1. Numerical tests

The computational domain consists of 20×20 bi-quadratic elements which correspond to 41×41 grid points. The bi-quadratic elements with lesser number of nodes smoothly capture the non-linear variations of the field vari-

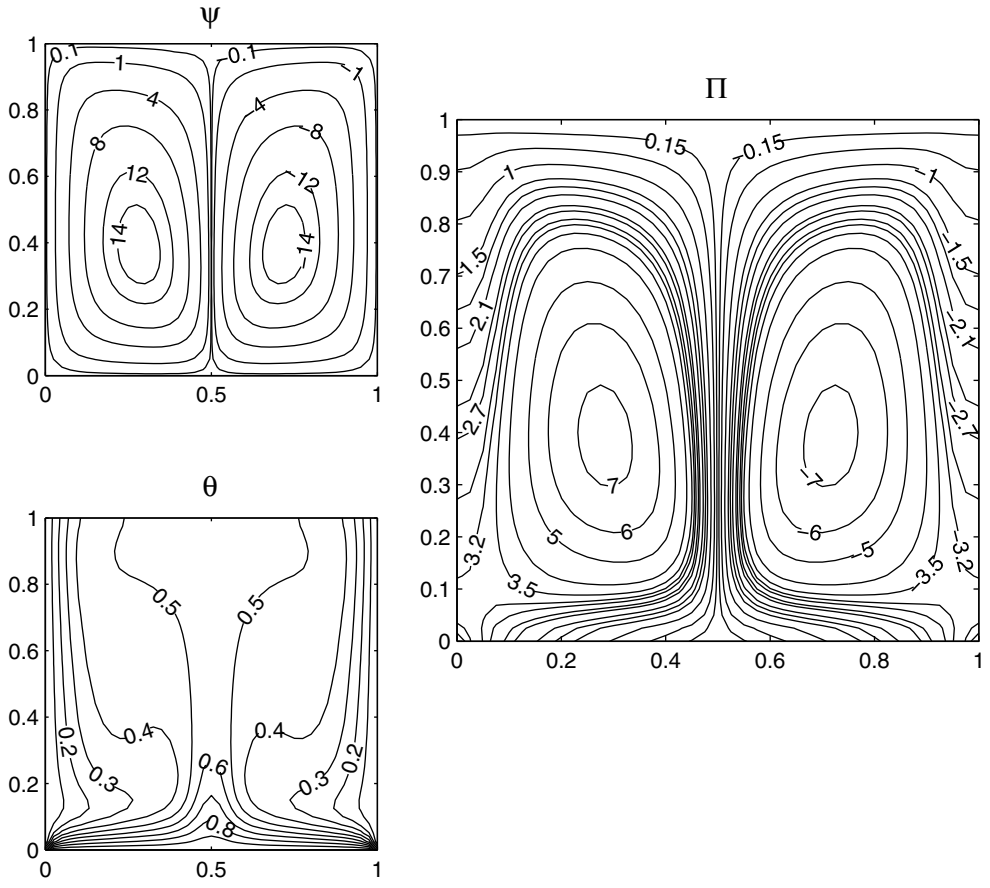

Fig. 6. Streamfunction (ψ), heatfunction (Π) and temperature (θ) contours for uniform heating corresponding to case 1 with $Pr = 1000$ and $Ra = 10^5$. Clockwise and anti-clockwise flows are shown via negative and positive signs of streamfunctions and heatfunctions, respectively.

ables which are in contrast with finite difference/finite volume solutions available in the literature [10–12]. In order to assess the accuracy of the numerical procedure, we have carried out computations based on the grid size (41×41) for a square enclosure filled with air ($Pr = 0.71$) subjected to hot left wall and cold right wall in presence of insulated horizontal walls at $Ra = 10^5$ as shown in Fig. 2 and the results are in well agreement with the previous work [30]. Although the homogeneous Neumann boundary conditions are valid (Eq. (22)) for the isothermal walls, but the uniqueness of the solution of Eq. (19) depends on Dirichlet conditions. Hence, $\Pi = 0$ is assumed at the bottom wall ($Y = 0, \forall X$) and consequently, $\Pi = \overline{Nu}$ (where $\overline{Nu}$ is the average Nusselt number) is obtained for the top wall ($Y = 1, \forall X$). In general, the Dirichlet boundary conditions for Π of adiabatic walls are naturally obtained for the test case via integrating Eq. (18). It is found that the average Nusselt number ($\overline{Nu}$) based on current methodology is 4.6 whereas $\overline{Nu} = 4.56$ was obtained in the previous work [30]. This situation involves high circulation at the center due to significant convection.

It is also observed that large number of heatlines appear near the hot left wall signifying high heat flux towards the cold right wall. The heatlines near the cold wall is almost horizontal signifying the conductive transport.

The sign of heatfunction needs special mention. The solution of heatfunction (Poisson equation) is strongly dependent on non-homogeneous Dirichlet boundary condition ($\Pi = \overline{Nu}$) and the sign of heatfunction is governed by the sign of 'non-homogeneous' Dirichlet condition. It is observed that near the top wall the sign of heatfunction is positive (as also assumed in the earlier work [30]) and the sign is negative in the core where the heatfunctions denote strong convective heat transfer. It may be noted that signs of streamfunction and heatfunction are identical for the convection dominated heat flows as also seen in Fig. 2. A detailed explanation for this situation may be found in earlier articles [23,30].

A detailed computations have been carried out for various values of Pr ($Pr = 0.026$–1000) and $Ra = 10^3$–10^5 with uniform and non-uniform heating of walls. For uniform heating situation, the jump discontinuities in Dirichlet type wall boundary conditions at the junction of hot and cold walls (see Fig. 1) correspond to computational singularities. In the current investigation, Gaussian quadrature based finite element method provides smooth solutions in the computational domain including the corner regions as evaluation of residuals depends on interior Gauss points and thus the effect of corner nodes are less pronounced in the final solution. Current solution scheme produces grid

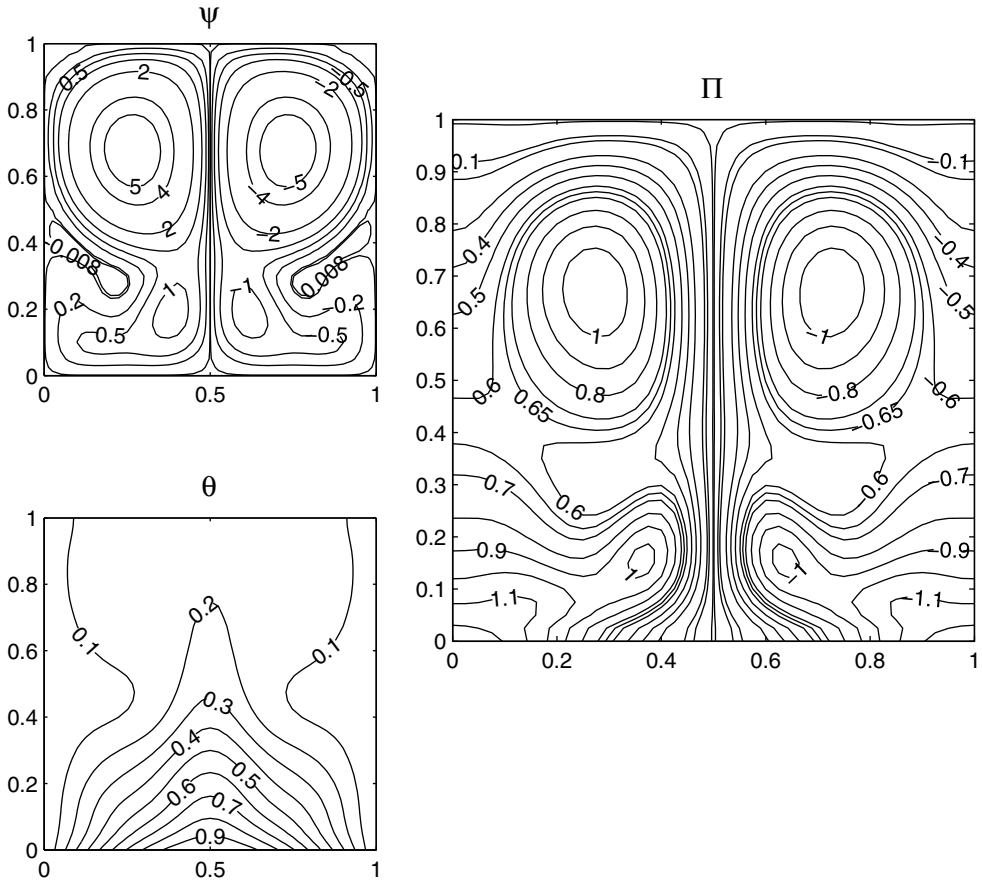

Fig. 7. Streamfunction (ψ), heatfunction (Π) and temperature (θ) contours for non-uniform (sinusoidal) heating corresponding to case 1 with $Pr = 0.026$ and $Ra = 10^5$. Clockwise and anti-clockwise flows are shown via negative and positive signs of streamfunctions and heatfunctions, respectively.

invariant results as discussed in our previous article [22]. The convergences tests have been carried out for all such cases and it is observed that 41×41 computational grids are adequate for smooth solutions.

3.2. Case 1: Uniform and non-uniform heating of bottom wall

Fig. 3 illustrates streamfunction, isotherms and heatfunctions for $Pr = 0.026$ and $Ra = 10^3$ with uniform heating of bottom wall in presence of cold side walls. Due to cold vertical walls, fluids rise up from middle portion of the bottom wall and flow down along two vertical walls forming two symmetric rolls inside the cavity as denoted by signs of streamfunctions. At $Ra = 10^3$, the magnitudes of streamfunctions are small signifying conduction dominant heat transfer within the cavity and the temperature contours are smooth lines which span the entire cavity.

The heatlines in Fig. 3 illustrate that the heat flow occurs mainly due to conduction as the heatlines are perpendicular to the cold or hot walls. The two bottom corner edges have infinite heat flux as the cold wall is directly in contact with the hot bottom wall. It may be noted that $\Pi = \overline{Nu_l} = 2.68$ at $X = 0, Y = 0$ and $\Pi = \overline{Nu_r} = -2.68$ at $X = 1, Y = 0$ and the sign of heatfunctions are dependent on these two corner boundary conditions. Our sign convention is based on the fact that the heat flow occurs from the hot to cold wall, and the positive heatfunction corresponds to anticlockwise heat flow. It may also be noted that, $\overline{Nu}$ denotes the total or cumulative heat flux at the two bottom corner points and therefore, the magnitudes of heatfunctions decrease from the bottom edges to the central symmetric line where the no heat flux condition is also valid due to symmetric boundary conditions for temperature.

It is interesting to observe that, heatline with $\Pi = 0.5$ connects within $X = 0.2$ and $Y = 0.25$ and that implies that more than 50% of the heat flux from the hot wall to cold wall is confined within the bottom portion of the cold wall. Consequently, the less heat flow occurs near the top portion of the cold walls. Therefore, the thermal boundary layer was found to develop near the bottom edges, and the thickness of boundary layer is larger at the top portion of the cold wall signifying less heat transfer from the hot wall. It may also be noted that as 50% heat energy flows from the regime $0 \leqslant X \leqslant 0.2$ and $1 \geqslant X \geqslant 0.8$ of the hot wall and the regime near to central regime of the hot wall remain hot as seen from parabolic temperature contours near the bottom wall. The heatlines clearly illustrate that the bottom portion of the cold wall receives most of heat energy from the hot wall whereas the top portion of the

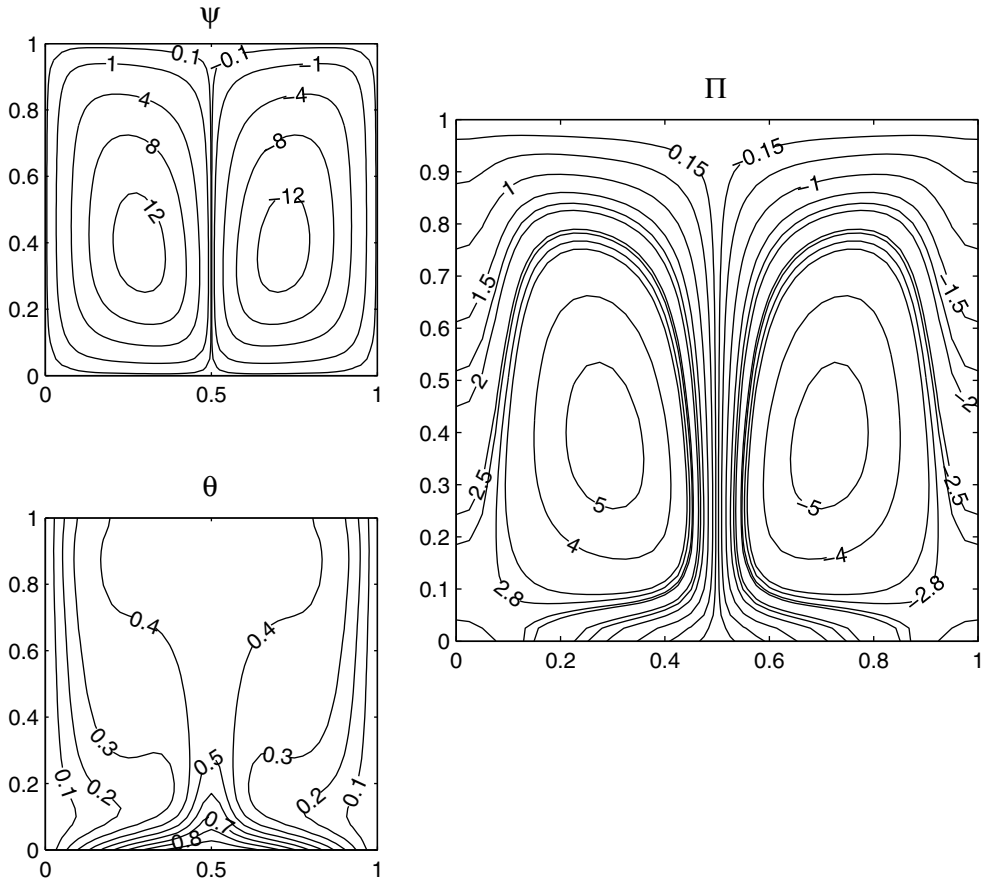

Fig. 8. Streamfunction (ψ), heatfunction (Π) and temperature (θ) contours for non-uniform (sinusoidal) heating corresponding to case 1 with $Pr = 1000$ and $Ra = 10^5$. Clockwise and anti-clockwise flows are shown via negative and positive signs of streamfunctions and heatfunctions, respectively.

cavity remains cool due to less transport of heat energy from the bottom wall. It is interesting to note that the fountain of heatlines from the central regime of the bottom wall is not strong enough to reach the regimes of top wall due to weak circulation and conduction dominated heat transfer.

Fig. 4 illustrates the streamfunction, heatfunction and isotherms for $Pr = 0.026$ and $Ra = 10^5$. At higher Ra, the intensity of fluid motion has been increased as indicated by larger magnitudes of streamfunctions. The primary vortex appears near the top wall whereas a weak secondary vortex appears near the bottom wall.

The enhanced convection causes larger heat energy to flow from the bottom wall to the top portion of the vertical wall. It may be noted that the significant convection causes distortion of heatlines as compared with conduction dominant heat transfer (see Fig. 3), and the shape of heatlines near the core is identical with the streamlines signifying the convection dominant heat flow due to large intensity of circulations as shown with large values of streamfunctions.

It is interesting to note that highly dense heatlines occur at the central regime of the cavity and the dense heatlines signify the larger heat flow. The vertical walls with $1 \geqslant Y \geqslant 0.58$ correspond to $\Pi = 0$–0.6 illustrating the significant heat flow whereas the regime with $0.58 \geqslant Y \geqslant 0.45$ correspond to $\Pi = 0.6$–0.65 which signifies small heat absorption. The lower portion of the vertical wall ($0 \leqslant Y \leqslant 0.35$) receives heat from the hot bottom wall as Π varies within 0.7–2.89. Therefore, the top and bottom portions of the vertical walls are hotter than the central regime of the vertical wall as seen in temperature contour plots. The heatlines near two corners of the bottom wall are almost circular which signifies that the conduction is dominant in those regimes. The multiple cells of heatlines near the top and bottom portions are due to multiple circulation cells. The secondary vortex recirculates heat energy from the central regime. The stronger primary vortex enhances the mixing process and therefore uniform temperature distribution occurs near the upper portion of the central regime. Hence, this regime has insignificant thermal gradient as θ varies within 0.2–0.3.

Fig. 5 shows the streamfunction, heatfunction and isotherms for $Pr = 0.7$ and $Ra = 10^5$. The intensity of fluid motion has been found stronger than that with $Pr = 0.026$. It may be noted that the maximum magnitude of the streamfunction is around 6 with $Pr = 0.026$ whereas the maximum values is around 14 with $Pr = 0.7$. It is also interesting to observe that the single symmetric vortex patterns with eyes near the center of each half occur for $Pr = 0.7$.

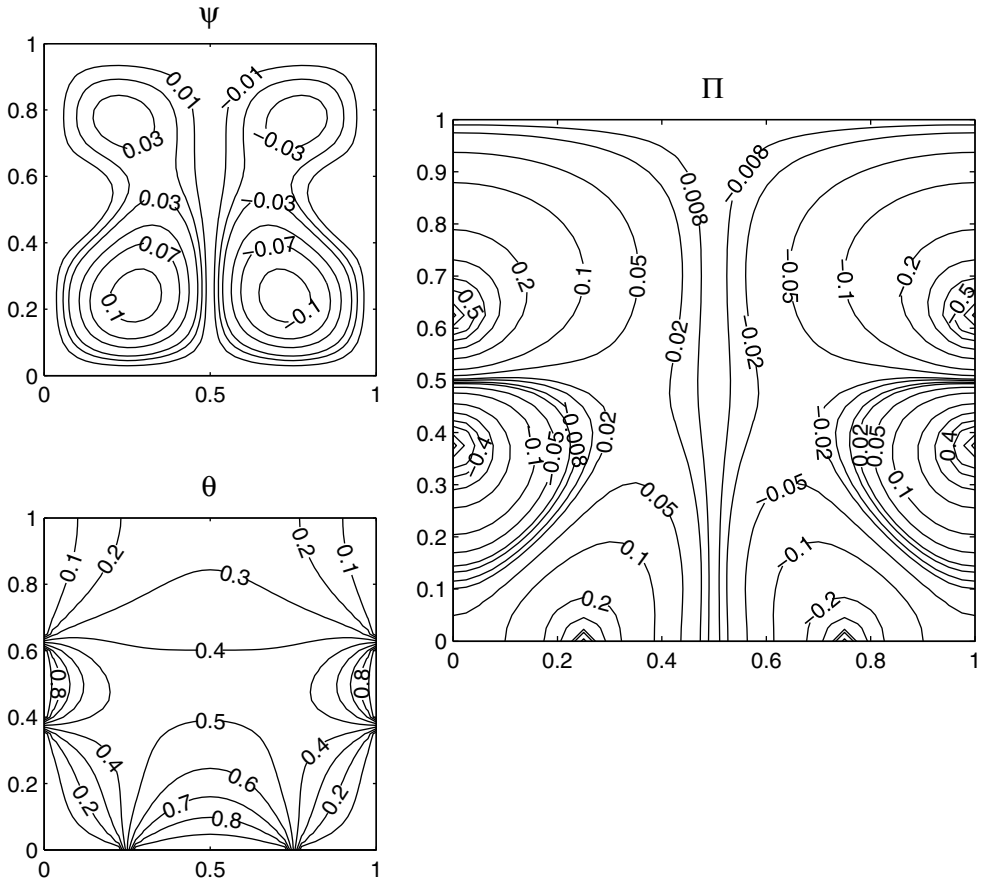

Fig. 9. Streamfunction (ψ), heatfunction (Π) and temperature (θ) contours for uniform heating corresponding to case 2 with $Pr = 0.026$ and $Ra = 10^3$. Clockwise and anti-clockwise flows are shown via negative and positive signs of streamfunctions and heatfunctions, respectively.

The enhanced convection due to larger Pr is reflected in heat flows as seen in heatline distributions. Similar to previous case with $Pr = 0.026$, the central regime consists of dense heatlines which signify large amount of heat flow due to enhanced convection. It is interesting to observe that the upper regime of each vertical wall ($1 \geqslant Y \geqslant 0.5$) receive larger heat as Π varies within 0–2.1 whereas Π varies within 2.1–2.7 for the lower portion ($0.5 \geqslant Y \geqslant 0.1$). Therefore, temperature contours are stretched towards the vertical wall near the regime which corresponds to $1 \geqslant Y \geqslant 0.4$. It may also be noted that the conduction regime occurs near a very small portion of two corners of the bottom wall due to enhanced convection. Due to dense heatlines from the hot bottom wall, the isotherms are also pushed towards the bottom wall and the regime near the bottom wall is cooler than that for $Pr = 0.026$ with $Ra = 10^5$. Due to increased circulation near the central regime, the heatlines at the central regime are dense and that reflect maximal heat transfer or enhanced thermal mixing in the central regime resulting in large uniform temperature as seen in isotherm contour plots. The temperature at the top portion of the central regime vary within 0.4–0.45. It is also interesting to note that due to enhanced circulations, the heatlines show large magnitudes of heatfunctions, and consequently, the temperature contour with $\theta = 0.4$ is pushed towards the cold vertical wall. As a final remark, the top portion of the cold wall receives heat from the bottom wall and this regime also receive heat due to enhanced circulations. As a result, large thermal boundary layer thickness occurs near the regime $Y = 0.2$.

Fig. 6 shows the distributions for $Pr = 1000$ and $Ra = 10^5$. It is observed that streamfunction and heatfunction contours are similar to the case with $Pr = 0.7$. However, it is interesting to observe that the eyes of vortices occur near the bottom portion of the wall as higher Pr implies lower thermal diffusivity. Due to circulations with larger intensity as seen with higher values of heatfunction compared to the previous cases, the thermal boundary layers are suppressed near two corners of the bottom wall as seen in Fig. 6. The convective heat transfer as illustrated with higher values of heatfunctions causes enhanced thermal mixing and 50% of the regime (near the top portion) remain at $\theta = 0.4$–0.5.

Figs. 7 and 8 show streamfunction, heatfunction and temperature distributions for non-uniform heating of bottom wall with $Pr = 0.026$–1000 and $Ra = 10^5$. For $Pr = 0.026$, the streamlines and heatlines exhibit qualitatively similar trends to the uniform heating case as seen in Figs. 4 and 7 and the maximum value of streamfunction is found to be 5 for both uniform and non-uniform heating

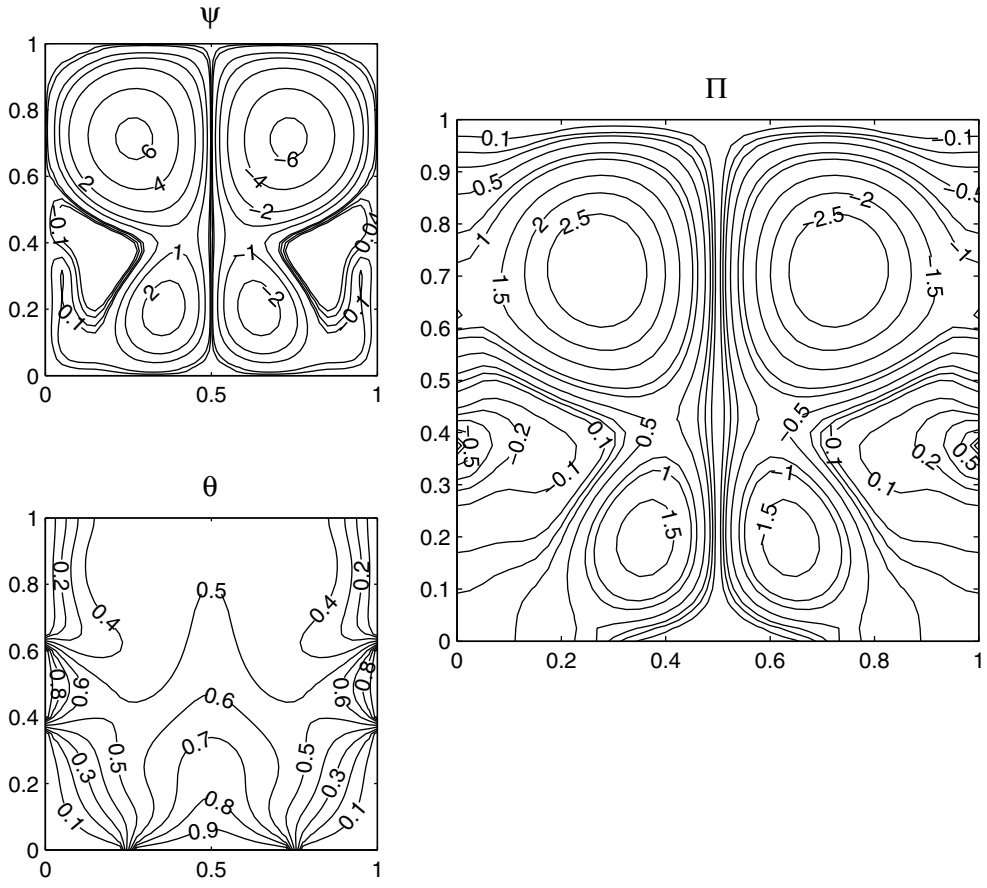

Fig. 10. Streamfunction (ψ), heatfunction (Π) and temperature (θ) contours for uniform heating corresponding to case 2 with $Pr = 0.026$ and $Ra = 10^5$. Clockwise and anti-clockwise flows are shown via negative and positive signs of streamfunctions and heatfunctions, respectively.

cases. It is observed that heatlines connect the regimes near to corner of bottom wall to the lower portion of the vertical wall up to $Y = 0.38$ and heatlines from $Y \geqslant 0.48$ connect to the central portion of the bottom wall. It is also interesting to observe that the heatlines are less dense near the top portion of the cavity as can be seen from heatline trajectories. Therefore, fluid is cooler than that with the uniform heating case at the top portion of the cavity as displayed by isotherm contours (see Figs. 4 and 7). Consequently, the temperature (θ) at the top portion of the central regime varies within 0.1–0.2. Due to non-uniform heating, the regimes near the bottom corner points are cold and that results in larger conduction regime for non-uniform heating case. Therefore, non-uniform heating may not be favorable for optimal circulation of heat energy for fluid with small *Pr*.

As *Pr* increases from 0.026 to 1000, in Figs. 7 and 8 it is found that the heatline contours become dense along the central regime, i.e., the heat flow becomes higher and the larger part of the top portion of the vertical wall receives heat energy from the bottom wall. However, in any case, uniform heating causes higher temperature near the top central regime than non-uniform heating. In addition, larger conduction regime and less dense contours occur near the bottom corners for non-uniform heating situations. Therefore, these regimes remain cooler irrespective of *Pr* and *Ra*.

It is observed that the temperature rise in the top portion of the central regime is up to 50% of the temperature of the bottom wall for both uniform and non-uniform heating cases. This is due to the fact that the smaller heat flow from the bottom wall is confined within the top portion of the vertical wall. In addition, the eyes of convective circulation cell is pushed towards the bottom wall for larger *Pr* at higher *Ra*. In order to achieve enhanced thermal mixing near the central core (which would be useful for food sterilization) studies on the role of distributed heating of both vertical walls and bottom walls have been carried out as discussed in the next section.

3.3. Case 2: Distributed uniform heating at bottom and vertical walls

Fig. 9 illustrates streamfunction, heatfunction and temperature distribution for $Pr = 0.026$ and $Ra = 10^3$. It may be noted that the uniform heat source is applied at $0.25 \leqslant X \leqslant 0.75$ for the bottom wall and at $0.375 \leqslant Y \leqslant 0.625$ for both the vertical walls. Common to cases 1 and 2 with uniform heating are the identical total heat sources. The importance of case 2 is based on the role

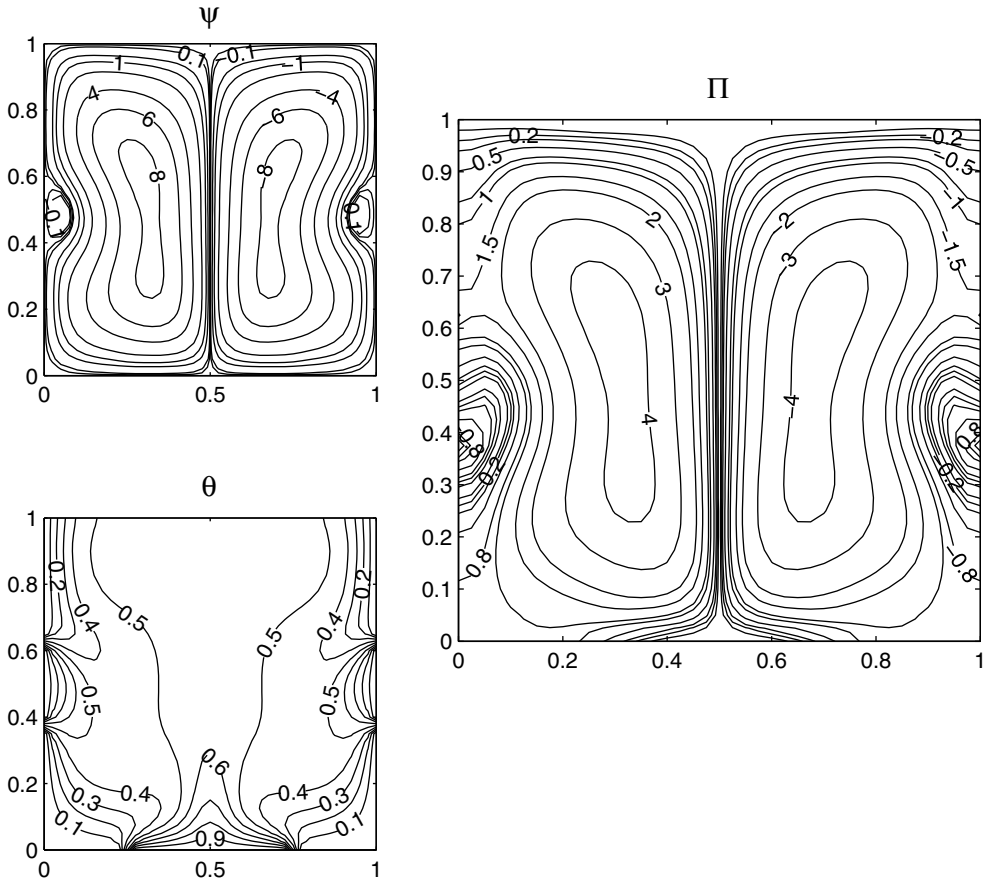

Fig. 11. Streamfunction (ψ), heatfunction (Π) and temperature (θ) contours for uniform heating corresponding to case 2 with $Pr = 1000$ and $Ra = 10^5$. Clockwise and anti-clockwise flows are shown via negative and positive signs of streamfunctions and heatfunctions, respectively.

of distributed heat sources for the global heatline trajectories. Similar to case 1, the intensity of flow circulation is smaller signifying conduction dominant heat flow within the cavity. Due to distributions of heat source at the center of vertical walls, multiple circulation cells, however small, tend to develop near the top and bottom walls. The temperature distributions show several closed loop contours bounded across the hot walls as seen in Fig. 9. It is also observed that the temperature contours within the domain are smooth lines due to conduction dominant heat transfer. The visualization of heat flow via heatlines are quite non-trivial due to islands of heat sources along the vertical and bottom walls and not yet reported in literature. As mentioned earlier, the unique solution of heatfunctions (Eq. (19)) depend on the exactness of Dirichlet boundary conditions and for case 2, the Dirichlet conditions are required at the junctions of cold-hot sectors as given by Eqs. (24).

The heatlines in Fig. 9 illustrate that heat flow mainly occur from the central regimes of the bottom and vertical walls. The heatlines are dense near the bottom half of the central heat source of the vertical wall. It may be noted that the regimes near the bottom corner receive the heat flux both from the vertical and bottom walls. Therefore, the maxima in θ is found as 0.4 near bottom corners. In contrast, the heatlines are less dense near the top portion of vertical walls. In addition, very few heatlines from the bottom wall reach to a very small regime of top portion of vertical walls. Therefore, the temperature near the top portion of the vertical wall varies within 0.1–0.2. It is interesting to note that, the top portion of the central regime corresponds to $\theta = 0.3$–0.4 due to distributed heat sources even with conduction dominant heat transfer. Most of the heatlines near the central regime of the hot bottom wall are confined within the bottom wall and the bottom portion of the vertical wall due to larger regime of heat source at bottom wall. It is also observed that, a larger portion near the central regime of the bottom wall corresponds to $\theta = 0.5$–1.

Fig. 10 illustrates the streamfunction, heatfunction and temperature distribution for $Pr = 0.026$ and $Ra = 10^5$. Due to combined effect of distributed heat sources and enhanced convection, multiple circulation cells occur near the top, bottom and vertical walls. The enhanced convection and multiple circulation cells cause the isotherm to be compressed along the walls. It is interesting to observe that the temperature within the central regime varies within 0.5–1 and this illustrates the enhanced thermal mixing which is predominantly due to distributed heating effects.

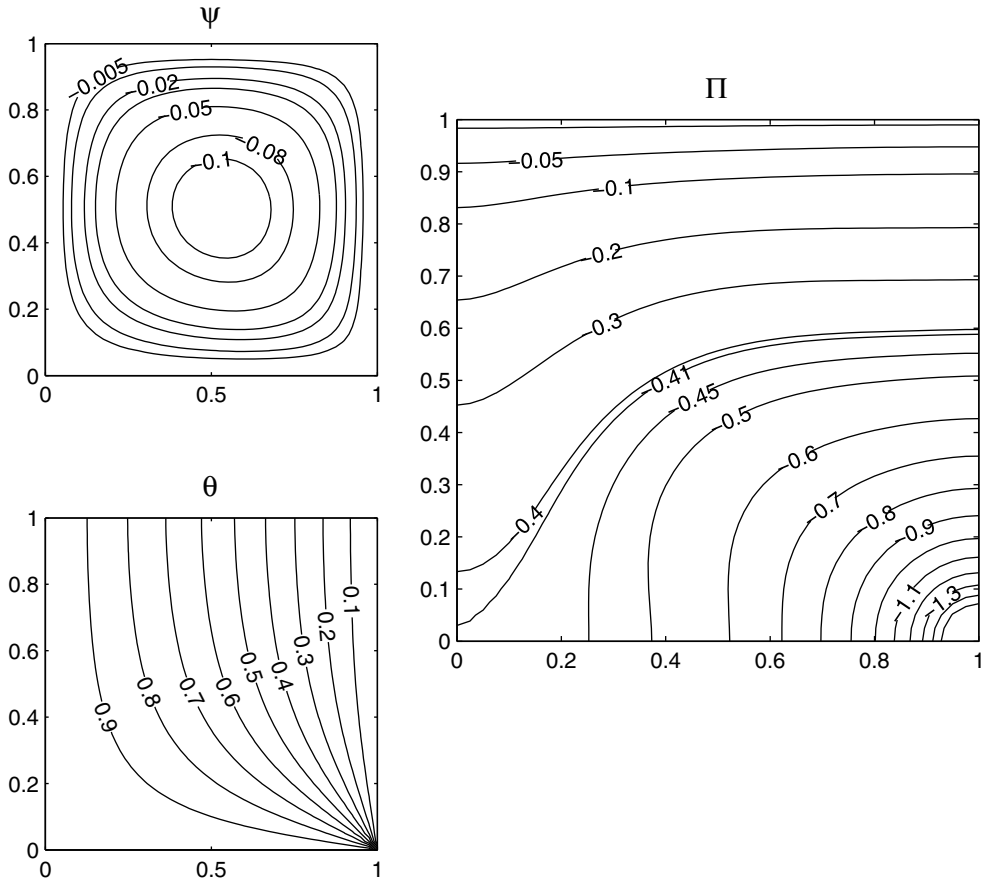

Fig. 12. Streamfunction (ψ), heatfunction (Π) and temperature (θ) contours for uniform heating corresponding to case 3 with $Pr = 0.026$ and $Ra = 10^2$. Clockwise and anti-clockwise flows are shown via negative and positive signs of streamfunctions and heatfunctions, respectively.

Further, the heatline contours would be useful to explain the heat flux distribution throughout the cavity.

The heatlines clearly illustrate the heat flux distributions from hot walls to the cold walls throughout the domain. It is observed that the heatlines from the central regime of the bottom wall ($0.25 \leqslant X \leqslant 0.75$) are distributed within $0.87 \leqslant Y \leqslant 1$ at the vertical wall. It is interesting to note that larger amount of heat is transported from the bottom wall to the top portion due to enhanced convective heating effect for $Ra = 10^5$. The central hot regime of the vertical walls ($0.375 \leqslant Y \leqslant 0.625$) distributes heat a small portion of the top portion of the vertical wall. Also, the heat flux from the hot portion of the vertical wall is distributed to the bottom portion of the cold regime of the vertical wall as well as cold regimes of the bottom wall. This induces enhanced thermal mixing leading to larger heat distributions to the cold regimes. In contrast, the heat from bottom wall is distributed at both vertical walls and near the bottom corner points for case 1. The heat flows are also observed from the vertical wall both at top and bottom portions for $Ra = 10^3$ due to conduction dominant heat transfer (see Fig. 9).

Fig. 11 illustrates the distributions for $Pr = 1000$ and $Ra = 10^5$. The strength of circulations is larger due to high Pr. It is also observed that similar to $Pr = 0.026$, the secondary circulation appears due to heated middle portion of the vertical wall. Due to enhanced buoyancy effects, the intensity of primary circulation cells is larger and the secondary circulation cells get suppressed for $Pr = 1000$. It is interesting to observe that the temperature contours are compressed to the side and bottom walls, and a large portion of the central regime corresponds to $\theta = 0.5$–0.6. The enhanced thermal mixing is further explained with the distributions of heatlines. The enhanced convection distributes large amount of heat at the top portion of the vertical walls and it is observed that the regime with $0.6 \leqslant Y \leqslant 1$ has the heatlines with magnitudes varying within 0–2. The large amount of heat is transferred to this regime due to heat transport from the hotter regime of bottom and side walls. The hot portion of side walls distributes heat up to the regime near to bottom corner points. Although the enhanced convection with larger heat energy distribution occurs with $Pr = 1000$, but the regime near the bottom corners remains cold as this regime does not receive heat from hot walls which contrast the situation with $Pr = 0.026$.

A very small regime near the bottom corners contain the cold fluid. However, due to overall larger heat distributions, the temperature in the core regime of the enclosure is larger than that with case 1 for identical Pr and Ra.

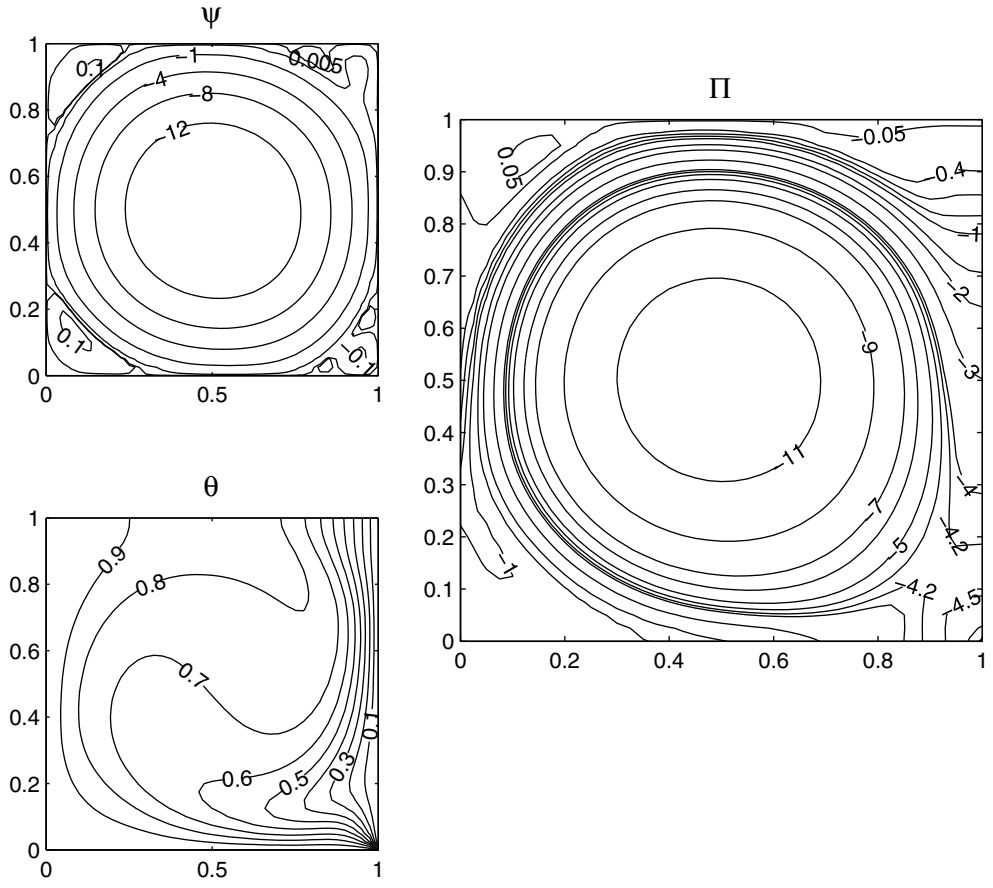

Fig. 13. Streamfunction (ψ), heatfunction (Π) and temperature (θ) contours for uniform heating corresponding to case 3 with $Pr = 0.026$ and $Ra = 10^5$. Clockwise and anti-clockwise flows are shown via negative and positive signs of streamfunctions and heatfunctions, respectively.

The temperature contours illustrate that the temperature in the core varies within 0.5–0.9 whereas the temperature in the core varies within 0.3–0.9 for case 1.

3.4. Case 3: Uniform heating of bottom wall and left vertical wall

Fig. 12 illustrates the streamfunction, heatfunction and temperature contours for $Pr = 0.026$ with $Ra = 10^2$. It is worthwhile to mention that the heat inputs are exactly two times than that for cases 1 and 2. Similar to cases 1 and 2, the intensity of flow circulation is smaller for $Ra = 10^2$ signifying the conduction dominant heat transfer and the isotherms are almost parallel except near the bottom wall. Consequently, the heatlines are almost parallel and they are perpendicular to hot/cold walls due to conduction dominant heat transfer. It is interesting to observe that the significant amount of heat flow from the hot vertical wall occurs from the regime with $1 \geqslant Y \geqslant 0.45$ and the magnitudes of heatfunctions vary within 0–0.3. In contrast, the bottom portion of hot vertical wall ($0.45 \leqslant Y \leqslant 0$) remain hotter as the heatfunctions vary within 0.3–0.42. The left half of the hot bottom wall ($0 \leqslant X \leqslant 0.5$) distribute less heat as heatfunctions vary within 0.42–0.6 whereas the right half has the heatfunction within 0.6–3.24. Therefore, a large portion near the left bottom corner remains hot due to less amount of heat flow. It is also interesting to observe that the upper portion of the cold wall ($1 \geqslant Y \geqslant 0.5$) receives lesser heat from the hot vertical wall as the magnitudes of heatfunction vary within 0–0.5 whereas the lower portion of the cold wall receives significant heat as magnitudes of heatfunctions vary within 0.5–3.24. Therefore the regime near to lower portion of the cold wall heats faster than the upper portion as also seen from temperature contours.

Fig. 13 illustrates streamfunction, heatfunction and temperature distributions for $Pr = 0.026$ and $Ra = 10^5$. Similar to Fig. 12, primary circulation cell occurs within the core. In addition, small secondary circulation cells also appear at the corner regimes. It may be noted that the maximum value of streamfunction is 12 due to high Ra. The large values of streamfunctions illustrate that the convection is dominant within the large regime of core. The enhance convective effect further influences the heat transport especially from the hot bottom wall. It may be noted that the regime in the bottom wall ($0.35 \leqslant X \leqslant 1$) distributes heat to a large regime of the cold wall ($0.75 \geqslant Y \geqslant 0$). On the other hand, the left hot wall distributes heat to a very small regime of the hot wall ($0.75 \leqslant Y \leqslant 1$). The convective transport of heat near the left top corner point also occurs

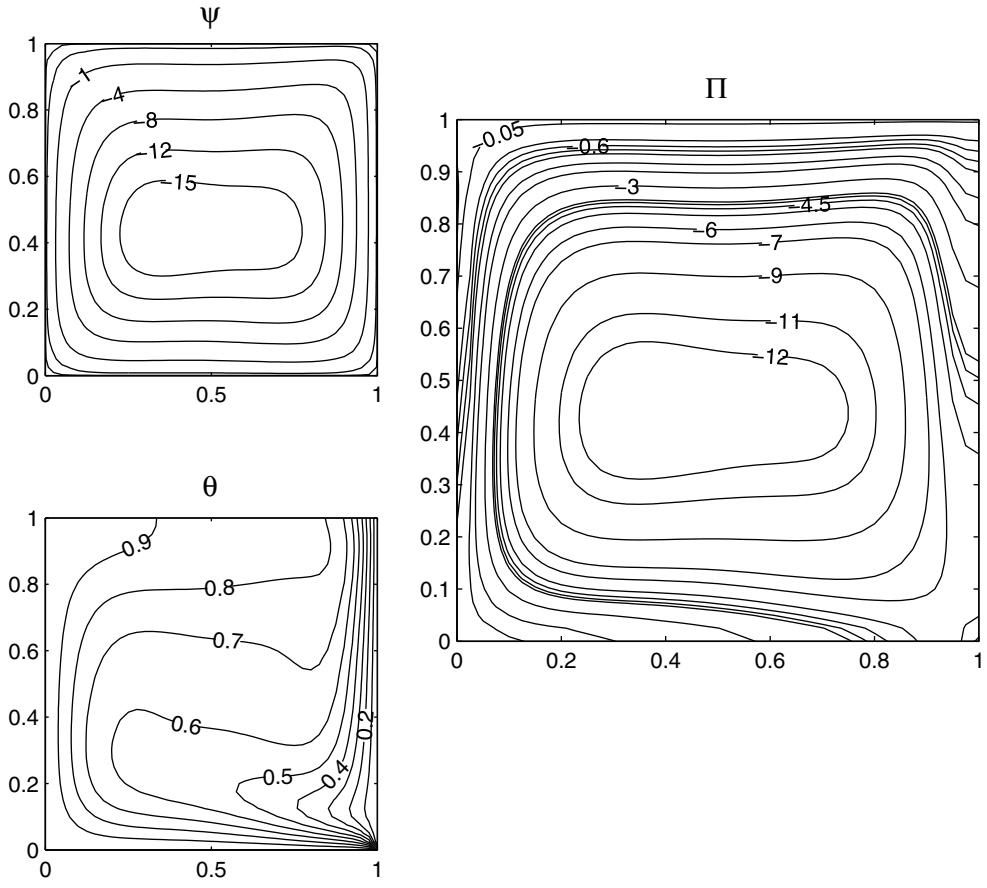

Fig. 14. Streamfunction (ψ), heatfunction (Π) and temperature (θ) contours for uniform heating corresponding to case 3 with $Pr = 1000$ and $Ra = 10^5$. Clockwise and anti-clockwise flows are shown via negative and positive signs of streamfunctions and heatfunctions, respectively.

due to secondary circulations. Compression of temperature contours are seen near the regime of the cold wall, $0.4 \leqslant Y \leqslant 0.8$, due to large amount of heat flow as seen from the dense heatlines in that regime. It may be interesting to note that conduction dominant regime occurs near the bottom portion of the cold wall and the amount of heat flow is also small. Therefore, the temperature contours are less compressed near bottom portion of the cold wall.

Fig. 14 illustrates the streamfunction, heatfunction and temperature contours for $Pr = 1000$ and $Ra = 10^5$. Similar to Fig. 13, a large primary circulation cell is found to occur, but secondary circulation cells are completely absent. Due to high Pr, the intensity of circulation is larger. The heatlines show similar features as that of Fig. 13. Due to larger convection, large amount of heat is transferred to the top portion of the cold wall. Therefore, temperature contours are more compressed at the top regime of cold wall for $Pr = 1000$ than that for $Pr = 0.026$. Overall, the temperature contours also illustrate that more than 70% of the enclosure has large temperature with $\theta = 0.6$–0.9 for higher Ra (see Figs. 13 and 14).

4. Conclusion

The heatlines and streamlines are extensively analyzed to demonstrate the heat flow for differentially and distributed heating of walls within cavities. The unique solutions of heatfunctions for differentially or distributed heating of walls are obtained for the first time in this work and the heat flow within the cavity is precisely governed by Dirichlet boundary conditions obtained from average Nusselt numbers for each hot or cold sector.

Initially, the enclosure with bottom heating in presence of two cold vertical walls and adiabatic top wall has been considered (case 1). The heat transfer is primarily conduction dominant for $Ra = 10^3$ and the regime near to bottom portion of the cold vertical walls corresponds to higher temperature due to large amount of heat flow from the bottom wall. The multiple circulation cells appear for $Pr = 0.026$ and multiple cells circulate heat within the central and bottom portions of the vertical walls. The strength of flow increases for fluid with larger Pr ($Pr = 0.7, 1000$) and at larger Pr, the secondary circulations disappear. At high Ra ($Ra = 10^5$), the top portion of the vertical wall receives heat from the bottom wall due to enhanced convective heating effects whereas the bottom portion of the cold wall continues to receive heat from the bottom wall. Although heat flow occurs along the central symmetric line up to the top portion of the vertical wall, but due to circulation, the heatlines show circular contours near the core where the heat flux is generally recirculated without heat transport from hot bottom wall. Therefore, the top portion of the central regime are at $\theta = 0.4$–0.5 and a large portion of near the cold walls remains at $\theta \leqslant 0.3$.

Based on the heatline trajectories, it has been decided to analyze the heating of fluid with distributed heat source at the bottom and side walls (case 2). The distributed heat source causes the heat flow from the hot regime to cold regime along both the vertical and bottom walls. Thus a large portion of the vertical wall receives heat energy either from central regimes of the bottom wall or from the central regimes of the vertical wall. Due to enhanced heat distribution the entire central regime is maintained at higher temperature with $\theta = 0.5$–0.7 especially at large Ra. Analysis also has been carried out with heated bottom and left vertical walls (case 3). It is observed that the heated bottom wall distributes large amount of heat to the cold wall whereas the heated left wall distributes heat near the top portion of the cold wall. Due to enhanced heating of walls with case 3, the core is at large temperature whereas the cold fluid is observed at a small regime near the right corner.

The heatlines concept has been implemented for the first time which includes differentially heated cavities with various combination of heating sources. The heatlines trajectories are powerful to visualize the direction of heat flow and strategy of distributed heat source has been evolved as a direct consequence of 'Bejan's heatlines' concept. The food processing often requires food to be kept at a large temperature for a long time and heatline concept has been found immense importance to control heat flow via tuning various types of heat inputs at the walls.

Acknowledgement

Authors thank anonymous reviewers for critical comments and suggestions which improved the quality of the manuscript.

References

[1] J.M. Garrpeters, The neutral stability of surface-tension driven cavity flows subject to buoyant forces. 1. Transverse and longitudinal disturbances, Chem. Eng. Sci. 47 (5) (1992) 1247–1264.
[2] L.B. Wang, N.I. Wakayama, Control of natural convection in non- and low-conducting diamagnetic fluids in a cubical enclosure using inhomogeneous magnetic fields with different directions, Chem. Eng. Sci. 57 (11) (2002) 1867–1876.
[3] I.E. Sarris, I. Lekakis, N.S. Vlachos, Natural convection in a 2D enclosure with sinusoidal upper wall temperature, Numer. Heat Transfer, Part A – Appl. 42 (2002) 513–530.
[4] A. Ousegui, A. Le Bail, M. Havet, Numerical and experimental study of a natural convection thawing process, AIChE J. 52 (12) (2006) 4240–4247.
[5] O. Laguerre, D. Flick, Heat transfer by natural convection in domestic refrigerators, J. Food Eng. 62 (1) (2004).
[6] J. Patterson, J. Imberger, Unsteady natural convection in a rectangular cavity, J. Fluid Mech. 100 (1980) 65–86.
[7] V.F. Nicolette, K.T. Yang, J.R. Lloyd, Transient cooling by natural convection in a two-dimensional square enclosure, Int. J. Heat Mass Transfer 28 (1985) 1721–1732.
[8] J.D. Hall, A. Bejan, J.B. Chaddock, Transient natural convection in a rectangular enclosure with one heated side wall, Int. J. Heat Fluid Flow 9 (1988) 396–404.
[9] J.M. Hyun, J.W. Lee, Numerical solutions of transient natural convection in a square cavity with different sidewall temperature, Int. J. Heat Fluid Flow 10 (1989) 146–151.
[10] T. Fusegi, J.M. Hyun, K. Kuwahara, Natural convection in a differentially heated square cavity with internal heat generation, Numer. Heat Transfer, Part A 21 (1992) 215–229.

[11] J.L. Lage, A. Bejan, The *Ra–Pr* domain of laminar natural convection in an enclosure heated from the side, Numer. Heat Transfer, Part A 19 (1991) 21–41.
[12] J.L. Lage, A. Bejan, The resonance of natural convection in an enclosure heated periodically from the side, Int. J. Heat Mass Transfer 36 (1993) 2027–2038.
[13] C. Xia, J.Y. Murthy, Buoyancy-driven flow transitions in deep cavities heated from below, ASME Trans. J. Heat Transfer 124 (2002) 650–659.
[14] M. November, M.W. Nansteel, Natural convection in rectangular enclosures from below and cooled along one side, Int. J. Heat Mass Transfer 30 (1987) 2433–2440.
[15] A. Valencia, R.L. Frederick, Heat transfer in square cavities with partially active vertically walls, Int. J. Heat Mass Transfer 32 (1989) 1567–1574.
[16] M.M. Ganzarolli, L.F. Milanez, Natural convection in rectangular enclosures heated from below and symmetrically cooled from the sides, Int. J. Heat Mass Transfer 38 (1995) 1063–1073.
[17] S. Kimura, A. Bejan, Natural convection in a differentially heated corner region, Phys. Fluids 28 (10) (1985) 2980–2989.
[18] O. Aydin, A. Unal, T. Ayhan, Natural convection in rectangular enclosures heated from one side and cooled from the ceiling, Int. J. Heat Mass Transfer 5 (1999) 2345–2355.
[19] A.T. Kirkpatrick, M. Bohn, An experimental investigation of mixed cavity natural convection in the high Rayleigh number regime, Int. J. Heat Mass Transfer 29 (1986) 69–82.
[20] M. Corcione, Effects of the thermal boundary conditions at the sidewalls upon natural convection in rectangular enclosures heated from below and cooled from above, Int. J. Therm. Sci. 42 (2003) 199–208.
[21] T. Basak, S. Roy, A.R. Balakrishnan, Effects of thermal boundary conditions on natural convection flows within a square cavity, Int. J. Heat Mass Transfer 49 (23-24) (2006) 4525–4535.
[22] S. Roy, T. Basak, Finite element analysis of natural convection flows in a square cavity with non-uniformly heated wall(s), Int. J. Eng. Sci. 43 (8–9) (2005) 668–680.
[23] S. Kimura, A. Bejan, The heatline visualization of convective heat-transfer, J. Heat Transfer – Trans. ASME 105 (4) (1983) 916–919.
[24] A. Bejan, Convection Heat Transfer, Wiley, New York, 1984.
[25] F.L. Bello-Ochende, A heat function formulation for thermal convection in a square cavity, Int. Commun. Heat Mass Transfer 15 (1988) 193–202.
[26] V.A.F. Costa, Unification of the streamline, heatline and massline methods for the visualization of two-dimensional transport phenomena, Int. J. Heat Mass Transfer 42 (1) (1999) 27–33.
[27] V.A.F. Costa, Heatline and massline visualization of laminar natural convection boundary layers near a vertical wall, Int. J. Heat Mass Transfer 43 (20) (2000) 3765–3774.
[28] V.A.F. Costa, Unified streamline, heatline and massline methods for the visualization of two-dimensional heat and mass transfer in anisotropic media, Int. J. Heat Mass Transfer 46 (8) (2003) 1309–1320.
[29] V.A.F. Costa, Bejan's heatlines and masslines for convection visualization and analysis, Appl. Mech. Rev. 59 (3) (2006) 126–145.
[30] Q.H. Deng, G.F. Tang, Numerical visualization of mass and heat transport for conjugate natural convection/heat conduction by streamline and heatline, Int. J. Heat Mass Transfer 45 (11) (2002) 2373–2385.
[31] A. Bejan, Convection Heat Transfer, third ed., Wiley, New York, 2004.
[32] A.M. Morega, Magnetic field influence on the convective heat transfer in the solidification processes, Part 2, Rev. Roum. Sci. Tech. – Electrotech. Energ. 33 (2) (1988) 155–156.
[33] A.M. Morega, The heat function approach to the thermomagnetic convection of electroconductive melts, Rev. Roum. Sci. Tech. – Electrotech. Energ. 33 (4) (1988) 359–368.
[34] S.K. Aggarwal, A. Manhapra, Use of heatlines for unsteady buoyancy-driven flow in a cylindrical enclosure, J. Heat Transfer – Trans. ASME 111 (1989) 576–578.
[35] D. Littlefield, P. Desai, Buoyant laminar convection in a vertical cylindrical annulus, J. Heat Transfer – Trans. ASME 108 (4) (1986) 814–821.
[36] C.J. Ho, Y.H. Lin, Thermal-convection heat-transfer of air water layers enclosed in horizontal annuli with mixed boundary-conditions, Warme Stoffubertragung – Thermo Fluid Dynam. 24 (4) (1989) 211–224.
[37] C.J. Ho, M.S. Wu, J.B. Jou, Analysis of buoyancy-aided convection heat-transfer from a horizontal cylinder in a vertical duct at low Reynolds-number, Warme Stoffubertragung – Thermo Fluid Dynam. 25 (6) (1990) 337–343.
[38] C.J. Ho, Y.H. Lin, Natural-convection of cold water in a vertical annulus with constant heat-flux on the inner wall, J. Heat Transfer – Trans. ASME 112 (1) (1990) 117–123.
[39] H. Chattopadhyay, S.K. Dash, Numerical visualization of convective heat-transfer from a sphere – with and without radial mass efflux, Int. J. Numer. Methods Heat Fluid Flow 5 (8) (1995) 705–716.
[40] A.M. Morega, A. Bejan, Heatline visualization of forced-convection laminar boundary-layers, Int. J. Heat Mass Transfer 36 (16) (1993) 3957–3966.
[41] A.M. Morega, A. Bejan, Heatline visualization of forced-convection in porous-media, Int. J. Heat Mass Transfer 15 (1) (1994) 42–47.
[42] S.K. Dash, Heatline visualization in turbulent flow, Int. J. Numer. Methods Heat Fluid Flow 6 (4) (1996) 37–46.
[43] J.N. Reddy, An Introduction to the Finite Element Method, McGraw-Hill, New York, 1993.
[44] G.K. Batchelor, An Introduction to Fluid Dynamics, Cambridge University Press, 1993.